



# Bamboo shoots shaped FeVO<sub>4</sub> passivated ZnO nanorods photoanode for improved charge separation/transfer process towards efficient solar water splitting

Xuefeng Long, Lili Gao, Feng Li, Yiping Hu, Shenqi Wei, Chenglong Wang, Tong Wang, Jun Jin\*, Jiantai Ma\*

State Key Laboratory of Applied Organic Chemistry (SKLAOC), The Key Laboratory of Catalytic Engineering of Gansu Province College of Chemistry and Chemical Engineering, Lanzhou University, Lanzhou, Gansu, 730000, PR China

## ARTICLE INFO

### Keywords:

FeVO<sub>4</sub>  
Heterojunction  
Surface states  
Photoelectrochemical water splitting  
ZnO nanorods

## ABSTRACT

Among many novel and promising semiconductors, the triclinic iron vanadate (FeVO<sub>4</sub>) has been rarely applied in the field of solar water splitting due to its poor charge carrier separation ability. In this work, we prepared FeVO<sub>4</sub>-passivated ZnO heterojunction nanorods (FVO/ZnO NRs) photoanodes by simple spin-coating and calcination method for the first time. The optimal photoanode exhibits stable and effective PEC water oxidation performance, compared to pristine ZnO, affording 130 mV negative shift in onset potential and 2.4 folds augment in photocurrent density. Particularly, X-ray photoelectron spectroscopy and Mott-Schottky test reveal the establishment of heterojunction, which subdue photo-induced carriers bulk recombination and improve the charge separation efficiency. Open-circuit photovoltage and electrochemical impedance spectroscopy were recorded to further clarify that the FeVO<sub>4</sub>-passivated layer eliminates the surface trapping state, thus increasing the photovoltage and promoting the interface charge transfer kinetics. These demonstrations are expected to provide new thread for the rational application of new photoanode candidates and to optimize PEC performance.

## 1. Introduction

It is essential to quest green, efficient and cheap sustainable energy source to replace contaminated traditional fossil fuels. As an inexhaustible, self-sustainable and clean energy source, solar energy has received significant attention [1,2]. In recent years, great efforts have been invested in how to harness solar energy efficiently, and photoelectrochemical (PEC) water splitting is a powerful approach for converting solar energy into chemical energy (hydrogen energy) [3,4].

In water splitting process, the water oxidation reaction involves the transfer of four-electrons to generate oxygen ( $2\text{H}_2\text{O} \rightarrow 4\text{H}^+ + \text{O}_2 + 4\text{e}^-$ ), and the kinetic is sluggish [5]. Hence, it still has a challenge to develop a highly efficient, inexpensive and durable photoanode material. Among many metal oxide semiconductors reported previously (such as TiO<sub>2</sub> [6,7], hematite [8–10], BiVO<sub>4</sub> [11,12], WO<sub>3</sub> [13,14], etc.), TiO<sub>2</sub> is the earliest [15] and most studied photocatalyst. However, the fast recombination and quenching of photo-induced charge carriers greatly affects solar energy conversion efficiency negatively. After long-term exploration efforts, zinc oxide (ZnO) has been believed to substitute TiO<sub>2</sub> to create promising photoanode thanks to its similar band level to

that of TiO<sub>2</sub> and an electron mobility nearly 100 times higher than that of TiO<sub>2</sub> [16,17]. On the basis of coating ZnO nanoparticle seeds, Yang and co-workers [18] controllably synthesized vertical ZnO nanorods array by the hydrothermal method. This one-dimensional structure has a high surface area and supplies a faster axial transport pathway for photo-induced holes [19], so as to reduce the recombination loss of photo-induced electron-hole pairs and encourage the transfer of holes to the surface active sites for water oxidation reaction.

Nevertheless, as a typical n-type wide band-gap semiconductor (~3.37 eV), the light absorption range of ZnO is restricted to the ultraviolet region [20]. Unfortunately, the photo-induced carriers cannot be easily separated owing to its large exciton binding energy (60 meV) [21]. It is generally acknowledged that developing nano heterostructure composite is an effective avenue to solve these problems. Recently, plentiful efforts have been injected into ZnO heterojunction engineering, such as ZnO/ZnS/g-C<sub>3</sub>N<sub>4</sub> [22], ZnO/BiVO<sub>4</sub> [23–25], ZnO/Fe<sub>2</sub>O<sub>3</sub> nanowire (NW) arrays [26], 3D ZnO/TiO<sub>2</sub>/FeOOH [27], 3D-branched ZnO/CdS NW arrays [28], ZnO/ZnSeO<sub>3</sub>/CuSeO<sub>3</sub> [29], ZnO/CdS/CdTe [30], and our previously reported O<sub>v</sub>-CoO<sub>x</sub>/ZnO nanorod arrays [31]. These efforts are all aimed at promoting photo-induced

\* Corresponding authors.

E-mail addresses: [jinjun@lzu.edu.cn](mailto:jinjun@lzu.edu.cn) (J. Jin), [majiantai@lzu.edu.cn](mailto:majiantai@lzu.edu.cn) (J. Ma).



carrier separation and improving the PEC performance of ZnO-based photoanode, but still have room for development. Especially, since ZnO is an amphoteric oxide, the experimental conditions for directly growing other materials on its surface are relatively harsh, and the current studied composite semiconductor heterostructure cannot achieve satisfactory effects, so it is essential to develop a new material to introduce into ZnO-based photoanode.

Iron (III) vanadate ( $\text{FeVO}_4$ ) is a novel and seldom studied n-type indirect band-gap semiconductor ( $E_g = 2.0\text{--}2.1\text{ eV}$ ) [32–34] in the field of PEC. Benefiting from its excellent chemical stability and high selectivity,  $\text{FeVO}_4$  has been used in the realm of photocatalytic degradation of organic pollutants [35,36] and catalytic dehydrogenation [37]. Through high-throughput screening methods,  $\text{FeVO}_4$  was first considered a promising photoanode material [33,38]. The theoretical maximum solar to hydrogen efficiency of  $\text{FeVO}_4$  is 16%, notwithstanding, its photocurrent density for PEC water oxidation reaction is still small (less than  $0.1\text{ mA cm}^{-2}$ ) [39], this is owing of its low mobility ( $\sim 5 \times 10^{-5}\text{ cm}^2\text{ V}^{-1}\text{ s}^{-1}$ ) and short diffusion length ( $\sim 2\text{ nm}$ ), which lead to fast bulk charge carriers recombination [33,40]. Through literature research [41,42],  $\text{FeVO}_4$  has a suitable band position to match well with ZnO to construct heterojunction interface, thereby facilitating the separation of charge carriers and improving the PEC performance of ZnO-based photoanodes. Revealingly, although there have been extensive studies on ZnO-based composite photoelectrode, the application of ZnO and  $\text{FeVO}_4$  type II heterojunction photoanode in PEC water splitting has still not been reported.

In the present work,  $\text{FeVO}_4$ -passivated ZnO heterojunction nanorods (FVO/ZnO NRs) photoanode were prepared for the first time through simple and inexpensive spin-coating followed by calcination method, and its PEC properties were explored. The physical and chemical properties of the as-prepared composite photoanode were characterized explicitly. Further, PEC measurement results revealed that, compared with pristine ZnO NRs, the FVO/ZnO NRs photoanode without loading any co-catalyst has a negative shift of  $130\text{ mV}$  in onset potential and  $2.4$  times augment in photocurrent density. Meanwhile, the target photoanode also has higher stability and more effective electrode surface area. More in-depth, we discussed the mechanism of charge carrier separation and transfer in detail, and verified it by Mott-Schottky (M-S), open circuit photovoltage (OCP) and electrochemical impedance spectroscopy (EIS) measurements.

## 2. Experimental section

### 2.1. Synthesis of ZnO NRs photoanode

The FTO substrates with a size of  $2.0 \times 1.0\text{ cm}$  were cleaned with acetone, ethanol and water successively before use. Synthesis of ZnO NRs photoanode was realized through spin-coating ZnO seed layer and hydrothermal method according to our previously reported method [31].

### 2.2. Synthesis of FVO/ZnO NRs photoanode

In order to deposit  $\text{FeVO}_4$  onto ZnO nanorods surface, a simple spin-coating precursor solution containing  $\text{Fe}(\text{NO}_3)_3 \cdot 9\text{H}_2\text{O}$ ,  $\text{NH}_4\text{VO}_3$  and  $\text{C}_6\text{H}_8\text{O}_7$  followed by calcination was applied [40]. Briefly,  $0.01\text{ M}$   $\text{Fe}(\text{NO}_3)_3 \cdot 9\text{H}_2\text{O}$  and  $0.01\text{ M}$   $\text{C}_6\text{H}_8\text{O}_7$  solution were prepared, followed by being stirred for  $30\text{ min}$  at  $80^\circ\text{C}$  (referred to as solution A). At the same time, a  $0.01\text{ M}$   $\text{NH}_4\text{VO}_3$  solution was prepared and stirred at  $80^\circ\text{C}$  to completely dissolve (referred to as solution B). Next, an equal amount of solutions of A and B were mixed evenly. Then, the FVO/ZnO NRs photoanodes were prepared by spin-coating the mixed solution on the ZnO NRs substrates at  $3000\text{ rpm}$  for  $20\text{ s}$ . The cycle number of spin-coatings was set to  $1, 3, 5$  times, followed by annealing at  $500^\circ\text{C}$  for  $2\text{ h}$  in a nitrogen atmosphere at a heating rate of  $3^\circ\text{C min}^{-1}$ .

### 2.3. Synthesis of $\text{FeVO}_4$ photoanodes

Adding  $40\text{ }\mu\text{L}$  of *Nafion* in  $2\text{ mL}$  of the above mixed solution, and the  $\text{FeVO}_4$  film were deposited onto the FTO substrates by dip-coating the precursor solution for  $3$  times. Then the samples were baked at  $500^\circ\text{C}$  for  $2\text{ h}$  in a nitrogen atmosphere at a heating rate of  $3^\circ\text{C min}^{-1}$ .

### 2.4. Structural characterization

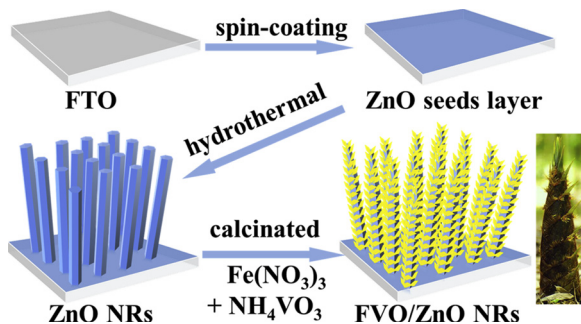
The thickness and surface morphology of photoanode were examined by a field emission scanning electron microscope (SEM) (HITACHI S-4800,  $5\text{ kV}$ ). Transmission electron microscopy (TEM) and high resolution TEM images (HR-TEM) measurement were conducted to obtain the microstructure of the samples, which was analysed using a field emission transmission electron microscope (FEI Talos F200S) operating at  $200\text{ kV}$ , combined with an energy dispersive X-ray spectrometer (EDS) for the determination of metal composition. The purity and the crystalline phase structure of all photoanodes were obtained using a Rigaku D/max-2400 power X-ray diffractometer with  $\text{Cu K}\alpha$  radiation as the X-ray source in ranging from  $20^\circ$  to  $90^\circ$ . X-ray photoelectron spectroscopy (XPS) measurements were conducted on a Kratos Axis Nova using monochromatized  $\text{Al K}\alpha$  X-ray source operated at  $15\text{ kV}$  and  $10\text{ mA}$  and referenced to the  $\text{C }1\text{s}$  peak ( $284.6\text{ eV}$ ). The light absorption abilities of all samples were measured with Ultraviolet-visible absorption spectra (Hitachi U-4000) in the range of  $300\text{--}800\text{ nm}$ , during which FTO glass as the reference for these absorption measurements. For steady-state photoluminescence (PL) spectra, a HITACHI F-7000 equipped with  $300\text{ nm}$  pulse laser radiation used as the excitation source at room temperature.

### 2.5. PEC measurements

All PEC measurements were operated using a conventional three-electrode configuration, which consisted of a platinum foil counter electrode, and  $\text{Ag}/\text{AgCl}$  reference electrode, and the  $0.5\text{ M}$   $\text{Na}_2\text{SO}_4$  ( $\text{pH } 6.5$ ) electrolyte. All photoanodes were illuminated under a  $\text{Xe } 300\text{ W}$  lamp (Perfect Light solar simulator). The simulated solar illumination was obtained through an AM 1.5 G filter and the light intensity was calibrated to  $100\text{ mW cm}^{-2}$  by a crystalline silicon solar cell (Photoelectric Instrument Factory of Beijing Normal University, Model FA-Z). The photocurrents under chopped light irradiation were obtained by linear sweep voltammetry (LSV) at a scan rate of  $10\text{ mV s}^{-1}$ . Electrochemical impedance spectra (EIS) measurement was collected with amplitude of  $5\text{ mV}$  at a bias of  $0.85\text{--}1.45\text{ V}$  vs. RHE with or without solar illumination over a frequency range from  $0.1\text{--}10^5\text{ Hz}$ . The impedance data was fit to an equivalent circuit model using the Zview software (Scribner Associates Inc., USA). Mott-Schottky (M-S) spectra were acquired in the potentials range of  $0$  to  $1.2\text{ V}$  vs. RHE in the dark condition at frequency of  $1\text{ kHz}$  and scan rate of  $20\text{ mV s}^{-1}$ . The incident photon-to-current conversion efficiency (IPCE) was measured at  $1.23\text{ V}$  vs. RHE by a monochromator between a  $300\text{ W}$  Xe lamp as the simulated light source and the PEC cell. The electrode potentials versus the reversible hydrogen electrode (RHE) are converted from the  $\text{Ag}/\text{AgCl}$  electrode using the equation:  $E_{\text{RHE}} = E_{\text{Ag/AgCl}} + 0.197 + 0.0591pH$ .

## 3. Results and discussion

As a typical demonstration, the fabrication process of FVO/ZnO NRs array photoanodes is depicted in **Scheme 1**. Vertically aligned ZnO NRs array was firstly grown on FTO substrate via a facile hydrothermal method based on the previous report [31], with smooth surface, uniform length of  $\sim 1.7\text{ }\mu\text{m}$  and the diameter approximately  $100\text{--}150\text{ nm}$  (**Fig. 1a, c** and **S1a**). Next, the  $\text{FeVO}_4$  precursor solution was spin-coated on the ZnO NRs, and the  $\text{FeVO}_4$ -modified ZnO NRs array photoanode was obtained after an annealing process in  $\text{N}_2$  atmosphere. From the scanning electron microscopy (SEM) and transmission electron



**Scheme 1.** Schematic diagram of the preparation procedure of the FVO/ZnO NRs photoanode.

microscopy (TEM) images of the FVO/ZnO NRs array (Fig. 1b, d and S1b), it can be seen that the diameter of FVO/ZnO NRs becomes wide, and numerous FeVO<sub>4</sub> nanoparticles aggregate on the upper part of ZnO NRs to form a loose and rough surface, and by observing the morphology of the contrast samples (Fig. S2b, c), it is found that as the number of spin-coating times of FeVO<sub>4</sub> precursors increase, the surface roughness and confusion degree increase. It serves to show from High-resolution TEM (HR-TEM) images (Fig. 1e) that FeVO<sub>4</sub> nanoparticles are attached to the edges of ZnO NRs, and the interplanar spacing of 0.260 nm matches well with the (002) plane of wurtzite phase ZnO [43]. Additionally, comparing the literature reports [42] and XRD standard card (PDF#38-1372) data, Fig. 1f exhibits the FeVO<sub>4</sub> spacing distance of 0.206 nm and 0.505 nm could be indexed to the (320) and (111) crystal plane of triclinic FeVO<sub>4</sub> structure. Moreover, the energy dispersive X-ray spectroscopy (EDS) elemental mapping results (Fig. 1g) confirm uniform distribution for Fe and V elements on the surface of ZnO NRs without aggregation, and there is no other detectable element signal in EDS data (Fig. S3).

As shown in Fig. S4a, the X-ray diffraction (XRD) diagram shows the typical ZnO diffraction peak corresponding to the wurtzite phase of PDF#36-1451 card. In addition, because of the relatively low concentration, the FeVO<sub>4</sub> coating does not display any obvious peak. In order to further confirm the existence of FeVO<sub>4</sub>, we determined the XRD of the FeVO<sub>4</sub> electrode (Fig. S4b). Compared with the FTO test results, it can be observed that there is a characteristic peaks apparently belonging to FeVO<sub>4</sub> at the position of 27.6°, corresponding to (2̄ 20) plane, and weak diffraction peaks appear at the positions of 25.0° and

42.7°. All the peaks are indexed to the triclinic structure, which are identical to the standard data (PDF#38-1372) [40].

The light harvesting capabilities were investigated using UV-vis diffuse reflectance spectra (UV-vis DRS), as presented in Fig. S5a. The sample of FVO/ZnO NRs presents a tail absorption band up to  $\approx$  550 nm compared to the absorption edge of pristine ZnO, indicating their enhanced light absorption. The FeVO<sub>4</sub> film is orange-yellow with an absorption edge of about 600 nm. The band gap energy of samples could be evaluated according to the Tauc plot  $a\hbar\nu = A(\hbar\nu - E_g)n/2$ , where  $a$ ,  $\hbar$ ,  $\nu$ ,  $A$  and  $E_g$  are the optical absorption coefficient, Planck constant, light frequency, optical absorbance and band gap energy, respectively. The value of  $n$  depends on the nature of the type of optical transition in the semiconductor [43]. For the direct band-gap semiconductor ZnO ( $n = 1$ ) [44], the calculated ZnO band gap is 3.22 eV (Fig. S5b). Nevertheless, the previous literature reported that FeVO<sub>4</sub> is an indirect band-gap semiconductor ( $n = 4$ ), as shown in Fig. S5c, the  $E_g$  is estimated to be 2.06 eV, which agrees with the values reported in the literature. Steady-state Photoluminescence (PL) emission spectrum were recorded to verify the charge carriers immigration, transfer and the recombination processes in the semiconductor [45]. As illustrated in Fig. S5d, an emission peak appears at 380 nm due to the edge exciton recombination, and the broad visible emission band are derived from defects state [46]. For FVO/ZnO NRs photoanodes, the emission peak intensity is significantly lower than that of pristine ZnO, indicating that FVO/ZnO heterojunction effectively decreased the photo-induced carriers recombination process [47].

The surface chemical composition and electronic states in the samples could be obtained by X-ray photoelectron spectroscopy (XPS) measurement. The wide region X-ray photoelectron spectrum manifests that the sample includes Zn, O, Fe and V elements (Fig. S6). Fig. 2a-d exhibit the fine spectra of the Zn 2p, O 1s, Fe 2p and V 2p core levels XPS scanned at high resolution, respectively. The doublet sharp peaks of Zn 2p<sub>3/2</sub> and Zn 2p<sub>1/2</sub> for ZnO NRs photoanode is located at 1021.32 and 1044.33 eV, respectively. After loading FeVO<sub>4</sub>-passivated layer to construct FVO/ZnO heterojunction photoanode, there is a slight positive shift (by 0.4 eV) in the Zn 2p binding energy, suggesting a decrease in its electron density [6,48]. Furthermore, the O 1s spectrum of FVO/ZnO heterojunction photoanode is deconvoluted into four sub-peaks at 529.60, 530.73, 531.54, and 532.85 eV, which are associated to the lattice oxygen atoms in V-O, Fe-O, Zn-O [42] and the surface-adsorbed OH species, respectively. It should be mentioned that the peaks of

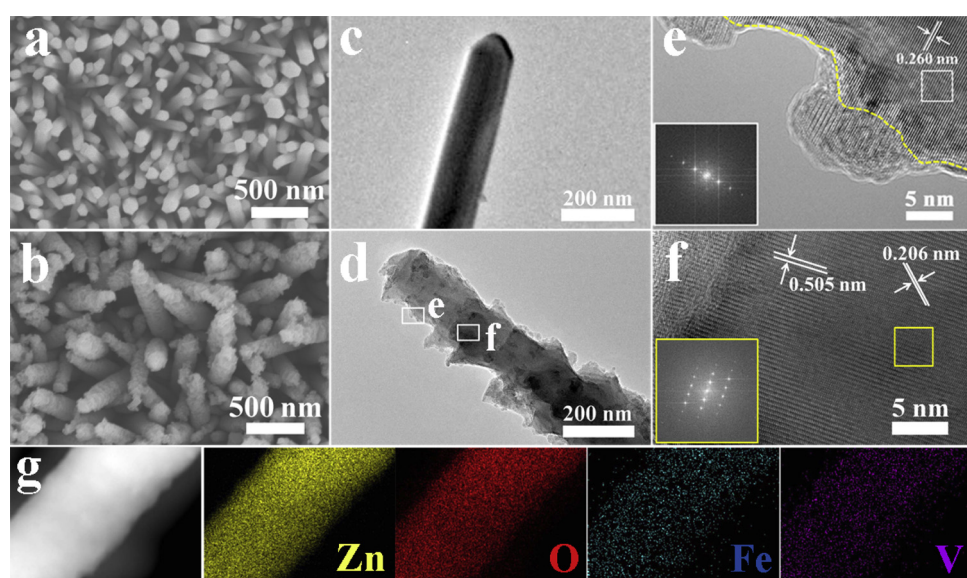


**Fig. 1.** Top-view SEM image of (a) vertically aligned pristine ZnO NRs array, and (b) FVO/ZnO NRs array on FTO. TEM image of (c) pristine ZnO NR and (d) FVO/ZnO NR. (e) and (f) typical HR-TEM images recorded from the marked area in (d). (g) EDS elemental mapping for Zn, O, Fe, and V of FVO/ZnO core-shell NRs.

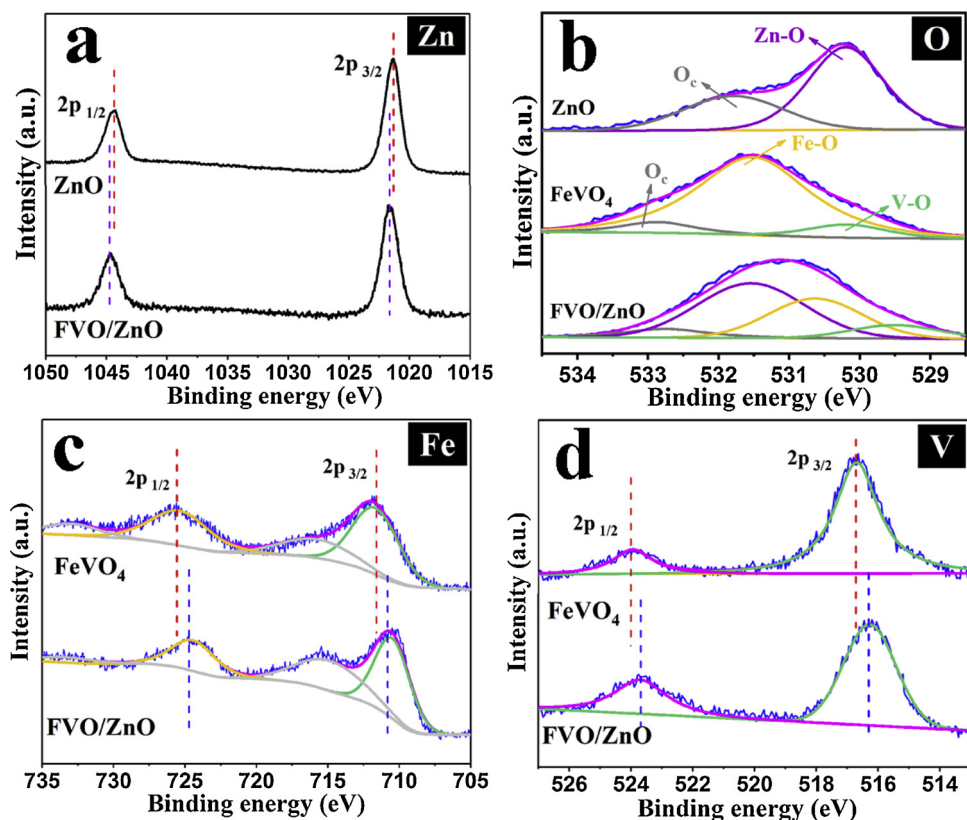


Fig. 2. Core-level XPS of (a) Zn, (b) O, (c) Fe, and (d) V elements.

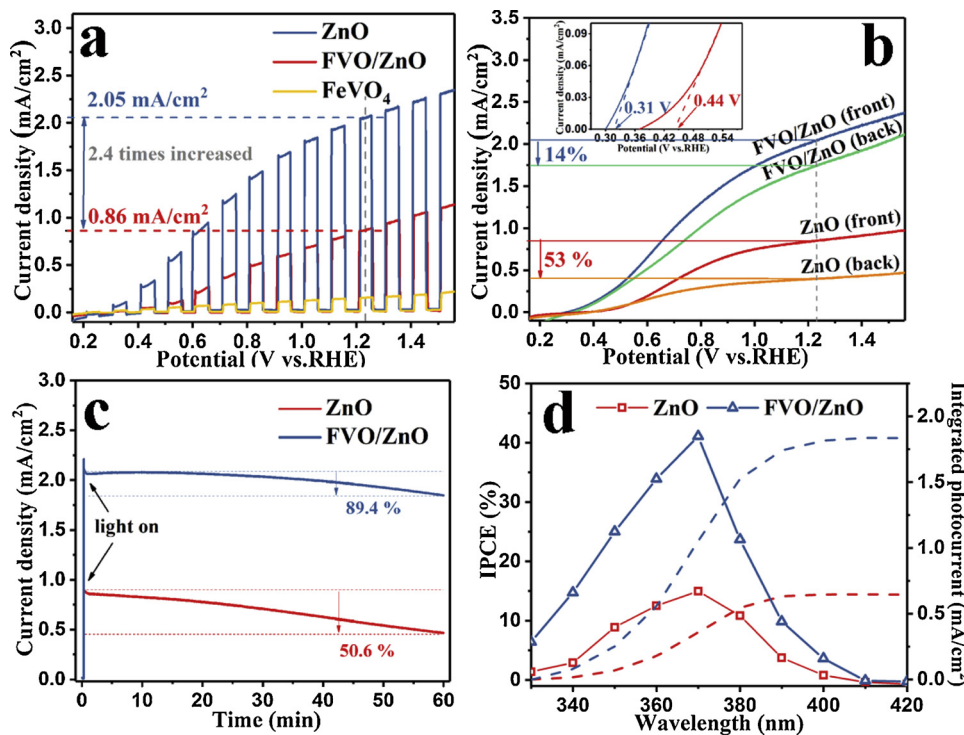
lattice oxygen atoms attributed to Zn–O shift to the high energy compared to ZnO NRs, inversely, Fe–O and V–O show a negative offset compared to that of FeVO<sub>4</sub> sample. Correspondingly, the FeVO<sub>4</sub> exhibits two peaks at 711.61 eV (Fe 2p<sub>3/2</sub>) and 725.58 eV (Fe 2p<sub>1/2</sub>) [36,49]. Meanwhile, only the Fe<sup>3+</sup> satellite peak appears and there are not Fe<sup>2+</sup> satellite peak at 715 or at 730 eV, demonstrating that the Fe element in the sample only exists in a trivalent oxidation state [50]. In addition, two peaks with binding energies of 516.74 eV and 524.02 eV are characteristic of V 2p<sub>3/2</sub> and V 2p<sub>1/2</sub>, which are in agreement with the state of V<sup>5+</sup> in FeVO<sub>4</sub> [33,51]. What's more, the peaks of Fe 2p and V 2p for the target FVO/ZnO photoanode both underwent negative shift (by ~0.5 eV), suggesting an increase in the electron density on the FeVO<sub>4</sub>. Visually, these binding energy shifts provide evidence of strong interfacial interactions between ZnO and FeVO<sub>4</sub>. In detailed, electron migrate from ZnO to FeVO<sub>4</sub> until both of Fermi levels align attains equilibrium, thereby built-in electric field from ZnO to FeVO<sub>4</sub> establish, which is in line with the typical type II heterojunction mechanism to facilitate the extraction of holes from the interior n-type domains to improve PEC performance.

For comparing the PEC performance for water splitting of ZnO NRs and FVO/ZnO NRs photoanode, Linear sweep voltammetry (LSV) curves have been studied in the 0.5 M Na<sub>2</sub>SO<sub>4</sub> (pH 6.5) solution without sacrificial reagent. As can be seen from Fig. 3a, the current density is immediately attenuated to negligible at the instant of turning off the light, additionally, the photocurrent density of FVO/ZnO NRs photoanode displays a great increase up to 2.05 mA cm<sup>-2</sup> at 1.23 V vs. RHE, which is 2.4 times that of pristine ZnO NRs under simulated solar irradiation. The PEC properties of contrast samples with different numbers of spin-coating times of FeVO<sub>4</sub> precursor have been tested in Supporting information (Fig. S2a), and the results indicate that the FVO/ZnO photoelectrode obtained by spin-coating three times of FeVO<sub>4</sub> precursor can achieve the maximum photocurrent density.

The separation and transfer properties of holes are analysed by comparing the difference in photocurrent between front-side and back-

side illumination [52] (details in the Supporting information). We experimentally found that the back-side photocurrent of the pristine ZnO NRs photoelectrode is 53% lower than the front-side photocurrent at 1.23 V vs. RHE (Fig. 3b), indicating for the hole near the bottom-end of the nanorod has extremely low utilization, and it is easy to be combined with photo-induced electrons. For the FVO/ZnO heterojunction photoanode, the difference in photocurrent between the front-side and back-side illuminations is reduced, revealing that the heterojunction can prevent photo-induced charge carrier from recombining in time, allowing more photo-induced holes to rapidly transfer into the electrolyte for water oxidation reaction. In addition, the onset potential of the FVO/ZnO photoanode (the inset in Fig. 3b) also exhibits enhanced PEC performance with a negative offset of 130 mV, benefiting from the effective photo-induced carriers separation by the built-in electric field in the heterojunction, as well as the lower electrode resistance and more active area, which will be discussed in detail later.

The stability of these photoanodes was evaluated using a chronoamperometry measurement under continuous irradiation for 3600 s and under chopped illumination for 400 s at a potential of 1.2 V vs. RHE. As presented in Fig. 3c, the photocurrent density of ZnO photoanode decreased by nearly half after the illumination of 3600 s, because ZnO is highly susceptible to severe chemical corrosion and photo-corrosion [20], while the photocurrent density of FVO/ZnO NRs photoanode is only reduced by 10%, demonstrating that the FeVO<sub>4</sub>-passivated layer could protect ZnO from corrosion and increase the stability of ZnO-based photoanode. From the SEM image of the FVO/ZnO photoanode after PEC testing (Fig. S7), it is clearly observed that the corrosion present around the circumference of ZnO NRs, indicating that a part of the sample is destroyed. Complementally, Fig. S8a displays that both ZnO NRs and FVO/ZnO NRs photoanodes exhibit a reproducible cyclic photocurrent response in the light on/off cycle during 400 s PEC water splitting, and an almost constant and non-attenuated photocurrent density can be attained per light cycle. In the meantime, their Faradaic efficiency for water oxidation was detected by gas



chromatography quantitatively (Fig. S8b). Compared with the calculated theoretical data, the actual measured yield of oxygen evolution is relatively low, and Faraday efficiency is approximately 91%.

To further quantitatively study the relationship between PEC performance and light absorption of the target photoanode, incident photon-current efficiency (IPCE) was examined at 1.23 V vs. RHE in a Na<sub>2</sub>SO<sub>4</sub> electrolyte. Fig. 3d exhibits that the IPCE of the photoanode is mainly concentrated in the UV region, and the tail absorption at 400–550 nm has little contribution to photocurrent conversion compared to the UV-vis absorption spectrum. The maximum IPCE value was obtained at 370 nm, which are 15% and 41% for ZnO and FVO/ZnO, respectively. The calculated integrated photocurrent densities (J<sub>c</sub>) of ZnO and FVO/ZnO NRs photoanodes are respectively 0.64 and 1.83 mA cm<sup>-2</sup>, which are matched with the LSV result. Additionally, as shown in Fig. S9, the maximum applied bias photon-to-current efficiency (ABPE) [53] of FVO/ZnO is up to approximately 0.56% at 0.78 V vs. RHE, which is 2.4 times higher than that of ZnO. These results are also in accord with the trend of the corresponding LSV curve.

Based on the above conclusion, it is speculated that the FVO/ZnO heterojunction photoelectrode exhibits enhanced PEC performance due to the establishment of built-in electric field from ZnO to FeVO<sub>4</sub>, which increases the photo-induced carriers separation efficiency, and the FeVO<sub>4</sub>-passivated layer may also increase the degree of band bending at the electrode-electrolyte interface, thus more photo-induced holes could participate in water oxidation reaction. In the following, combined with M-S, charge separation efficiency ( $\eta_{\text{sep}}$ ), charge injection efficiency ( $\eta_{\text{inj}}$ ), OCP and EIS tests specifically analyse the charge carriers separation/transfer in the bulk and interface.

First of all, in order to get insight into the underlying mechanism of the significant enhancement in the PEC performance of the photoanodes, M-S measurements were performed in 0.5 M Na<sub>2</sub>SO<sub>4</sub> solution with an applied frequency of 1 kHz in the dark (Fig. 4a). According to the M-S plots, flat band potential ( $E_{\text{fb}}$ ) and the carrier density ( $N_{\text{D}}$ ) of the photoelectrodes can be calculated using the Mott-Schottky equation [54,55]:

$$1/C_s^2 = (2/q\epsilon\epsilon_0 N_{\text{D}})[(E_{\text{app}} - E_{\text{fb}}) - kT/q]$$

**Fig. 3.** (a) Photocurrent density vs. applied potential curves in light on-off cycles. (b) Front and back side illumination photocurrents of pristine ZnO and FVO/ZnO photoanode under irradiation (100 mW cm<sup>-2</sup>). (c) Chronoamperometry of pristine ZnO and FVO/ZnO NRs photoanodes at a potential of 1.2 V vs. RHE under illumination in a period of 60 min. (d) IPCE curves and integrated photocurrent at 1.23 V vs. RHE for photoanodes.

$$N_{\text{D}} = (2/q\epsilon\epsilon_0)[d(1/C_s^2)/dE]^{-1}$$

Where q is elementary charge, k is the Boltzmann constant, T is the absolute temperature.  $\epsilon_0$  is the permittivity of vacuum,  $\epsilon$  is the dielectric constant of ZnO (10) [56].  $C_s$  is capacitance of the space charge region per unit area of the semiconductor; and  $E_{\text{app}}$  is the applied potential between the electrodes for M-S curves. What is noteworthy is that the Mott-Schottky equation is derived from the plate electrode, so these calculated the  $N_{\text{D}}$  and  $E_{\text{fb}}$  values are only used for comparison purposes [57].

As seen from Fig. 4a, all photoanodes are n-type conductivity because their M-S curves possess positive slopes [58]. According to the fitting line slope of the plots, as it is clear, the slopes of pristine FeVO<sub>4</sub> and FVO/ZnO photoanodes are smaller, and the  $N_{\text{D}}$  value of FVO/ZnO ( $5.69 \times 10^{20} \text{ cm}^{-3}$ ) is about three times that of ZnO ( $1.97 \times 10^{20} \text{ cm}^{-3}$ ), which is a vital contribution to improving the conductivity of ZnO and initiating photo-induced water splitting reaction. We speculate that it is due to the formation of an build-in electric field, so that more holes were transferred from ZnO bulk via FeVO<sub>4</sub> layer, thus resulting in less electron-hole recombination and a larger  $N_{\text{D}}$  value [59]. On the other hand, the passivation effect of the surface FeVO<sub>4</sub> coating effectively reduces the surface state density along with a decreased carrier recombination [60]. Beyond that, the  $E_{\text{fb}}$  of the electrode is also important to help to elucidate the semiconductor band structure and heterojunction [61], which ultimately determine whether the photoelectrode has the ability to drive water splitting. When the ZnO and FeVO<sub>4</sub> are in contact with each other, the majority carriers (electrons) in the ZnO with a more negative  $E_{\text{fb}}$  could diffuse to the FeVO<sub>4</sub> with a more positive  $E_{\text{fb}}$  until the flat band potentials attain equilibrium. In this way, an n-n type II heterojunction is formed. Simultaneously, excessive negative charges are accumulated near the FeVO<sub>4</sub> interface, and the ZnO interface exhibits electropositive, generating a built-in electric field in a direction from ZnO to FeVO<sub>4</sub>, which is in keeping with the conclusions drawn by XPS.

On the basis of the foregoing, we measured the photocurrent density in the electrolyte with 0.5 M Na<sub>2</sub>SO<sub>3</sub> sacrificial agent (Fig. S10) and then calculated  $\eta_{\text{sep}}$  (Supporting Information and Fig. S11 for details). The results are shown in Fig. 4b. Compared to the pristine ZnO

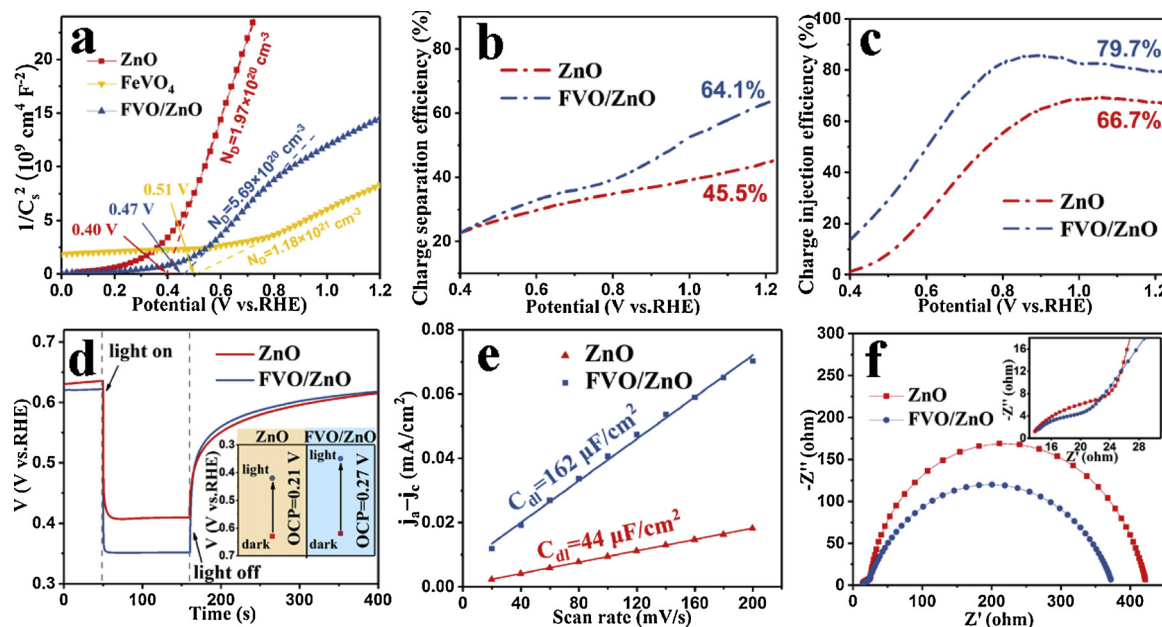


**Fig. 4.** (a) Mott-Schottky plots collected at a fixed frequency of 1 kHz, (b) Charge separation efficiency ( $\eta_{\text{sep}}$ ), (c) Charge injection efficiency ( $\eta_{\text{inj}}$ ), (d) Open circuit photovoltage curves, (e) Charging current differences ( $\Delta j = j_a - j_c$ ) measured at 0.31 V plotted against scan rate for each photoanode.  $j_a$  and  $j_c$  are the anodic and cathodic current, respectively, and the linear slope is twice of the double-layer capacitance ( $C_{\text{dl}}$ ), (f) Nyquist plots of the samples at 1.2 V vs. RHE under illumination. The large arc in the low frequency area represents  $R_{\text{ct,ss}}$ , while the small arc in the high frequency area (as shown in the illustration) represents  $R_{\text{bulk}}$ .

photoanode, the bulk charge separation efficiency of the target photoanode is up to 64% at applied bias of 1.23 V vs. RHE, meaning that the built-in electric field is very effective in the separation of photo-induced electron-holes pairs, and significantly inhibits the recombination of the charge carrier.

Furthermore, we also calculated  $\eta_{\text{inj}}$  (Fig. 4c) and in surprise found that the charge injection efficiency of the target electrode is significantly improved likewise. To investigate the surface carrier charge transfer process of the photoelectrodes, the open circuit photovoltage (OCP = OCP<sub>light</sub>-OCP<sub>dark</sub>) test was performed [7]. Essentially, the photovoltage is the difference between the quasi-electronic Fermi level ( $E_{F,n}$ ) and the quasi-hole Fermi level ( $E_{F,p}$ ), however, the presence of surface states causes the Fermi level pinning effect to bring about a decrease in photovoltage [62,63]. Clearly, as shown in Fig. 4d, the FVO/ZnO heterojunction photoanode has the larger OCP compared with the ZnO NRs electrodes, indicating that FeVO<sub>4</sub>-passivated layer have an influence on surface states elimination, which diminish Fermi level pinning behaviour, therefore would incur larger band bending and fast charge transfer at the electrode-electrolyte interface.

Based on the formation of the loose structure of the FVO/ZnO NRs photoanode surface, we suppose that the electrochemical active area of the composite photoanode may increase. Electrochemical double layer capacitance ( $C_{\text{dl}}$ ) of the samples at the non-Faradaic potentials (Fig. S12) are carried out to assess the effective electrode surface area (ECSA) of the photoanodes [64]. The results in Fig. 4e exhibit that the  $C_{\text{dl}}$  of the FVO/ZnO heterojunction photoanode is four times higher than that of the pristine ZnO NRs photoanode. Since ECSA is proportional to the  $C_{\text{dl}}$  of the photoanode, the FeVO<sub>4</sub>-passivated ZnO nanorod photoanode not only improves the carrier separation/transfer ability, but also increases the surface catalytic active area, which is also more favorable for the occurrence of water oxidation reaction.

Nyquist plot under illumination were recorded to get a deeper understanding of the charge transfer kinetics in the bulk and interface. The measured Nyquist plot (Fig. 4f) can be fitted with an equivalent circuit diagram (Fig. S13), which includes three resistances:  $R_{\text{series}}$ , series resistance in the PEC cell,  $R_{\text{bulk}}$ , charge transfer resistance in the bulk associated with the charge trapping and  $R_{\text{ct,ss}}$ , charge transfer resistance at the electrode-electrolyte interface associated with the hole

transfer process from surface states. As expected, the heterojunction (FVO/ZnO) achieves a lower  $R_{\text{bulk}}$  than pristine ZnO NRs (Fig. 4f and S14a), verifying that the building of the heterojunction is in favor of efficient charge separation, thereby subduing the recombination of photo-induced electron-holes pairs in the bulk and/or on surface states, which is accord with the calculated  $\eta_{\text{sep}}$  results. Interestingly, the optimal photoanode also exhibits a reduction of  $R_{\text{ct,ss}}$  (Fig. 4f and S14b). Corresponding to the analysis of the OCP test, our explanation is that the FeVO<sub>4</sub>-passivated layer is beneficial to remove the surface trapping state, and the larger band bending can boost the interface charge transfer kinetics, offsetting the external applied bias required to overcome the surface state recombination. Besides, the characteristic peak frequency of the FVO/ZnO NRs samples in the corresponding Bode phase plot (Fig. S15) is more negative than that of the pristine ZnO NRs, implying a longer carriers lifetime [65,66]. The result of this analysis indicates that the FVO/ZnO heterojunction helps to promote the charge separation/transfer and prolong photo-induced charge carriers lifetime.

In terms of the aforesaid analysis of charge separation/transfer of photoanode in the bulk and interface, we propose a possible band alignment model to describe the charge transfer behavior of FVO/ZnO photoanodes during PEC water oxidation. As displayed in Fig. 5a, photo-induced electron-hole pairs are easily recombined in the bulk and/or surface states for pristine ZnO NRs photoanodes. After modifying the FeVO<sub>4</sub>-passivated layer (Fig. 5b), on the one hand, the bulk conductivity is improved stemming from the high  $N_D$ , thereby benefiting for the bulk charge transfer capability. More importantly, the conduction band and the valence band of ZnO and FeVO<sub>4</sub> match well to form a type II heterojunction, which induce a built-in electric field to suppress photo-induced carriers recombination in the bulk, allowing more holes to transfer from the semiconductor to the electrode/electrolyte interface. On the other hand, the FeVO<sub>4</sub>-passivated layer weakens the Fermi level pinning effect caused by the surface trapping state, and thus increasing the photovoltage, which means providing a stronger surface reaction driving force while accelerating the interface charge transfer kinetics referring to  $R_{\text{ct,ss}}$ . As a consequence, the target photoanode exhibits excellent PEC properties with a larger photocurrent density and a more negative onset potential.

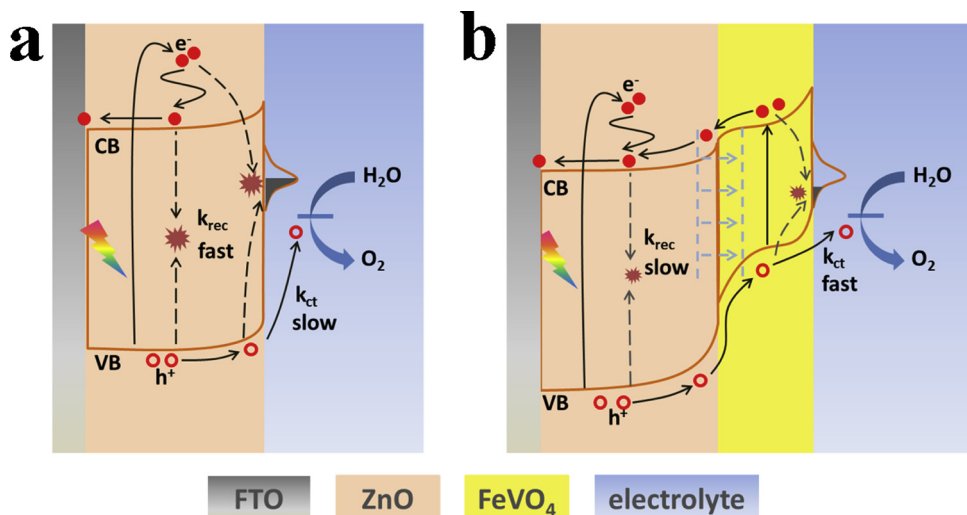


Fig. 5. Schematic band alignment of charge transport and recombination models in (a) ZnO and (b) FVO/ZnO photoanodes, where  $k_{rec}$  and  $k_{ct}$  represent photo-induced charge carriers recombination in the bulk and transfer at the electrode-electrolyte interface, respectively.

#### 4. Conclusions

In summary, we successfully fabricated FeVO<sub>4</sub>-passivated ZnO heterojunction nanorods (FVO/ZnO NRs) photoanode for the first time, and demonstrated the potential application value of FeVO as a novel photoanode material for solar water splitting. Under the condition of no co-catalyst and sacrificial reagent, the target photoelectrode is exhibited to be stable and efficient for water oxidation. AM1.5 G illumination photocurrent density of 2.05 mA cm<sup>-2</sup> at 1.23 V vs. RHE was generated, which increase more than 2.4 folds compared to the pristine ZnO NRs. Otherwise, both the onset potential and the IPCE are significantly improved. The improved performance is attributed to the effective promotion of bulk charge separation in the heterojunction between FeVO<sub>4</sub> and ZnO, and the FeVO<sub>4</sub>-passivated layer further results in larger photovoltage, which expedites the interface charge transfer kinetics while provides a stronger driving force for water oxidation reaction. Our experiments will stimulate research into the rational application of new photoanode candidates for solar water splitting.

#### Acknowledgements

This research was supported by the National Natural Science Foundation of China (21872066, 21773096), the Fundamental Research Funds for the Central Universities (Izujbky-2017-kb11), the Natural Science Foundation of Gansu (17JR5RA213), the Key Laboratory of Catalytic Engineering of Gansu Province and Resources Utilization, Gansu Province for financial support.

#### Appendix A. Supplementary data

Supplementary material related to this article can be found, in the online version, at doi:<https://doi.org/10.1016/j.apcatb.2019.117813>.

#### References

- [1] T. Yao, X. An, H. Han, J.Q. Chen, C. Li, Photoelectrocatalytic materials for solar water splitting, *Adv. Energy Mater.* (2018) 1800210.
- [2] G. Xie, K. Zhang, B. Guo, Q. Liu, L. Fang, J.R. Gong, Graphene-based materials for hydrogen generation from light-driven water splitting, *Adv. Mater.* 25 (2013) 3820–3839.
- [3] T. Wang, J. Gong, Single-crystal semiconductors with narrow band gaps for solar water splitting, *Angew. Chem. Int. Ed.* 54 (2015) 10718–10732.
- [4] M. Arif, G. Yasin, M. Shakeel, X. Fang, R. Gao, S. Ji, D. Yan, Coupling of bifunctional CoMn-layered double hydroxide@graphitic C<sub>3</sub>N<sub>4</sub> nanohybrids towards efficient photoelectrochemical overall water splitting, *Chem. – Asian J.* 13 (2018) 1045–1052.
- [5] R. Gao, H. Zhang, D. Yan, Iron diselenide nanoplatelets: stable and efficient water-electrolysis catalysts, *Nano Energy* 31 (2017) 90–95.
- [6] F. Ning, M. Shao, S. Xu, Y. Fu, R. Zhang, M. Wei, D.G. Evans, X. Duan, TiO<sub>2</sub>/graphene/NiFe-layered double hydroxide nanorod array photoanodes for efficient photoelectrochemical water splitting, *Energy Environ. Sci.* 9 (2016) 2633–2643.
- [7] H. Zhu, M. Zhao, J. Zhou, W. Li, H. Wang, Z. Xu, L. Lu, L. Pei, Z. Shi, S. Yan, Z. Li, Z. Zou, Surface states as electron transfer pathway enhanced charge separation in TiO<sub>2</sub> nanotube water splitting photoanodes, *Appl. Catal. B: Environ.* 234 (2018) 100–108.
- [8] Z. Zhou, S. Wu, L. Qin, L. Li, L. Li, X. Li, Modulating oxygen vacancies in Sn-doped hematite film grown on silicon microwires for photoelectrochemical water oxidation, *J. Mater. Chem. A* 6 (2018) 15593–15602.
- [9] Z. Luo, C. Li, S. Liu, T. Wang, J. Gong, Gradient doping of phosphorus in Fe<sub>2</sub>O<sub>3</sub> nanoarray photoanodes for enhanced charge separation, *Chem. Sci.* 8 (2017) 91–100.
- [10] F. Li, J. Li, F. Li, L. Gao, X. Long, Y. Hu, C. Wang, S. Wei, J. Jin, J. Ma, Facile regrowth of Mg-Fe<sub>2</sub>O<sub>3</sub>/P-Fe<sub>2</sub>O<sub>3</sub> homojunction photoelectrode for efficient solar water oxidation, *J. Mater. Chem. A* 6 (2018) 13412–13418.
- [11] S. Wang, T. He, J.-H. Yun, Y. Hu, M. Xiao, A. Du, L. Wang, New iron-cobalt oxide catalysts promoting BiVO<sub>4</sub> films for photoelectrochemical water splitting, *Adv. Funct. Mater.* (2018) 1802685.
- [12] G. Lili, L. Feng, H. Haiguo, L. Xuefeng, X. Na, H. Yiping, W. Shensi, W. Chenglong, M. Jianbai, J. Jun, Dual modification of BiVO<sub>4</sub> photoanode by constructing heterojunction with NiMoO<sub>4</sub> and depositing CoPi co-catalyst for enhanced photoelectrochemical performance, *ChemSusChem* 11 (2018) 2502–2509.
- [13] Z. Gu, L. Zhang, B. Wen, X. An, H. Lan, L.-M. Liu, T. Chen, J. Zhang, X. Cao, J. Tang, H. Liu, J. Qu, Efficient design principle for interfacial charge separation in hydrogen-intercalated nonstoichiometric oxides, *Nano Energy* 53 (2018) 887–897.
- [14] D. Jeon, N. Kim, S. Bae, Y. Han, J. Ryu, WO<sub>3</sub>/Conducting polymer heterojunction photoanodes for efficient and stable photoelectrochemical water splitting, *ACS Appl. Mater. Interfaces* 10 (2018) 8036–8044.
- [15] A. Fujishima, K. Honda, Electrochemical photolysis of water at a semiconductor electrode, *Nature* 238 (1972) 37–38.
- [16] A. Kargar, K. Sun, Y. Jing, C. Choi, H. Jeong, G.Y. Jung, S. Jin, D. Wang, 3D branched nanowire photoelectrochemical electrodes for efficient solar water splitting, *ACS Nano* 7 (2013) 9407–9415.
- [17] Z. Bai, X. Yan, Z. Kang, Y. Hu, X. Zhang, Y. Zhang, Photoelectrochemical performance enhancement of ZnO photoanodes from ZnIn<sub>2</sub>S<sub>4</sub> nanosheets coating, *Nano Energy* 14 (2015) 392–400.
- [18] L.E. Greene, M. Law, D.H. Tan, M. Montano, J. Goldberger, G. Somorjai, P. Yang, General route to vertical ZnO nanowire arrays using textured ZnO seeds, *Nano Lett.* 5 (2005) 1231–1236.
- [19] J. Han, Z. Liu, K. Guo, X. Zhang, T. Hong, B. Wang, AgSbS<sub>2</sub> modified ZnO nanotube arrays for photoelectrochemical water splitting, *Appl. Catal. B: Environ.* 179 (2015) 61–68.
- [20] J. Kegel, I.M. Povey, M.E. Pemble, Zinc oxide for solar water splitting: a brief review of the material's challenges and associated opportunities, *Nano Energy* 54 (2018) 409–428.
- [21] I. Khan, A. Qurashi, G. Berdiyorov, N. Iqbal, K. Fuji, Z.H. Yamani, Single-step strategy for the fabrication of GaON/ZnO nanoarchitected photoanode their experimental and computational photoelectrochemical water splitting, *Nano Energy* 44 (2018) 23–33.
- [22] C. Liu, Y. Qiu, F. Wang, K. Wang, Q. Liang, Z. Chen, Design of core-shell-structured ZnO/ZnS hybridized with graphite-like C<sub>3</sub>N<sub>4</sub> for highly efficient photoelectrochemical water splitting, *Adv. Mater. Interfaces* 4 (2017) 1700681.
- [23] S.J.A. Moniz, J. Zhu, J. Tang, 1D Co-pi modified BiVO<sub>4</sub>/ZnO junction cascade for efficient photoelectrochemical water cleavage, *Adv. Energy Mater.* 4 (2014)

1301590.

[24] D. Kim, Z. Zhang, K. Yong, Synergistic doping effects of a ZnO:N/BiVO<sub>4</sub>:Mo bunched nanorod array photoanode for enhancing charge transfer and carrier density in photoelectrochemical systems, *Nanoscale* 10 (2018) 20256–20265.

[25] L. Yan, W. Zhao, Z. Liu, 1D ZnO/BiVO<sub>4</sub> heterojunction photoanodes for efficient photoelectrochemical water splitting, *Dalton Trans.* 45 (2016) 11346–11352.

[26] Y.K. Hsu, Y.C. Chen, Y.G. Lin, Novel ZnO/Fe<sub>2</sub>O<sub>3</sub> core-shell nanowires for photoelectrochemical water splitting, *ACS Appl. Mater. Interfaces* 7 (2015) 14157–14162.

[27] Z. Li, S. Feng, S. Liu, X. Li, L. Wang, W. Lu, A three-dimensional interconnected hierarchical FeOOH/TiO<sub>2</sub>/ZnO nanostructural photoanode for enhancing the performance of photoelectrochemical water oxidation, *Nanoscale* 7 (2015) 19178–19183.

[28] Z. Bai, X. Yan, Y. Li, Z. Kang, S. Cao, Y. Zhang, 3D-branched ZnO/CdS nanowire arrays for solar water splitting and the service safety research, *Adv. Energy Mater.* 6 (2016) 1501459.

[29] T. Hong, Z. Liu, H. Liu, J. Liu, X. Zhang, J. Han, K. Guo, B. Wang, Preparation and enhanced photoelectrochemical performance of selenite-sensitized zinc oxide core-shell composite structure, *J. Mater. Chem. A* 3 (2015) 4239–4247.

[30] G. Kartopu, D. Turkay, C. Ozcan, W. Hadibrata, P. Aurang, S. Yerci, H.E. Unalan, V. Barrioz, Y. Qu, L. Bowen, A.K. Gürlek, P. Maiello, R. Turan, S.J.C. Irvine, Photovoltaic performance of CdS/CdTe junctions on ZnO nanorod arrays, *Sol. Energy Mater. Sol. Cells* 176 (2018) 100–108.

[31] X. Long, F. Li, L. Gao, Y. Hu, H. Hu, J. Jin, J. Ma, Heterojunction and oxygen vacancy modification of ZnO nanorod array photoanode for enhanced photoelectrochemical water splitting, *ChemSusChem* 11 (2018) 4094–4101.

[32] S.K. Biswas, J.-O. Baeg, Enhanced photoactivity of visible light responsive W incorporated FeVO<sub>4</sub> photoanode for solar water splitting, *Int. J. Hydrogen Energy* 38 (2013) 14451–14457.

[33] M. Zhang, Y. Ma, D. Friedrich, R. van de Krol, L.H. Wong, F.F. Abdi, Elucidation of the opto-electronic and photoelectrochemical properties of FeVO<sub>4</sub> photoanodes for solar water oxidation, *J. Mater. Chem. A* 6 (2018) 548–555.

[34] M. Balamurugan, G. Yun, K.-S. Ahn, S.H. Kang, Revealing the beneficial effects of FeVO<sub>4</sub> nanoshell layer on the BiVO<sub>4</sub> inverse opal core layer for photoelectrochemical water oxidation, *J. Phys. Chem. C* 121 (2017) 7625–7634.

[35] B. Ozturk, G.S. Pozan Soylu, Synthesis of surfactant-assisted FeVO<sub>4</sub> nanostructure: characterization and photocatalytic degradation of phenol, *J. Mol. Catal. A Chem.* 398 (2015) 65–71.

[36] J. Li, W. Zhao, Y. Guo, Z. Wei, M. Han, H. He, S. Yang, C. Sun, Facile synthesis and high activity of novel BiVO<sub>4</sub>/FeVO<sub>4</sub> heterojunction photocatalyst for degradation of metronidazole, *Appl. Surf. Sci.* 351 (2015) 270–279.

[37] Y. Li, S. Chen, A. Xu, F. Ma, F. Chen, W. Lu, Research on the nanocrystal FeV<sub>x</sub>O<sub>y</sub> catalysts for new reaction from propane to propylene and CO, *Appl. Surf. Sci.* 320 (2014) 552–557.

[38] T. Arai, Y. Konishi, Y. Iwasaki, H. Sugihara, K. Sayama, High-throughput screening using porous photoelectrode for the development of visible-light-responsive semiconductors, *J. Comb. Chem.* 9 (2007) 574–581.

[39] C.D. Morton, I.J. Slipper, M.J.K. Thomas, B.D. Alexander, Synthesis and characterisation of Fe–V–O thin film photoanodes, *J. Photochem. Photobiol. A: Chem.* 216 (2010) 209–214.

[40] W. Wang, Y. Zhang, L. Wang, Y. Bi, Facile synthesis of Fe<sup>3+</sup>/Fe<sup>2+</sup> self-doped nanoporous FeVO<sub>4</sub> photoanodes for efficient solar water splitting, *J. Mater. Chem. A* 5 (2017) 2478–2482.

[41] Z. Jiao, X. Guan, M. Wang, Q. Wang, B. Xu, Y. Bi, X.S. Zhao, Undamaged depositing large-area ZnO quantum dots/RGO films on photoelectrodes for the construction of pure Z-scheme, *Chem. Eng. J.* 356 (2019) 781–790.

[42] X. She, Z. Zhang, M. Baek, K. Yong, Elevated photoelectrochemical activity of FeVO<sub>4</sub>/ZnFe<sub>2</sub>O<sub>4</sub>/ZnO branch-structures via slag assisted-synthesis, *RSC Adv.* 7 (2017) 16787–16794.

[43] M. Arif, G. Yasin, M. Shakeel, M.A. Mushtaq, W. Ye, X. Fang, S. Ji, D. Yan, Hierarchical CoFe-layered double hydroxide and g-C<sub>3</sub>N<sub>4</sub> heterostructures with enhanced bifunctional photo/electrocatalytic activity towards overall water splitting, *Mater. Chem. Front.* 3 (2019) 520–531.

[44] K. Han, M. Xie, L. Zhang, L. Yan, J. Wei, G. Ji, Q. Luo, J. Lin, Y. Hao, C.-Q. Ma, Fully solution processed semi-transparent perovskite solar cells with spray-coated silver nanowires/ZnO composite top electrode, *Sol. Energy Mater. Sol. Cells* 185 (2018) 399–405.

[45] G. Xie, L. Guan, L. Zhang, B. Guo, A. Batool, Q. Xin, R. Boddula, S.U. Jan, J.R. Gong, Interaction-dependent interfacial charge-transfer behavior in solar water-splitting systems, *Nano Lett.* 19 (2019) 1234–1241.

[46] J.M. Li, H.Y. Cheng, Y.H. Chiu, Y.J. Hsu, ZnO-Au-SnO<sub>2</sub> Z-scheme photoanodes for remarkable photoelectrochemical water splitting, *Nanoscale* 8 (2016) 15720–15729.

[47] L. Wang, H. Hu, N.T. Nguyen, Y. Zhang, P. Schmuki, Y. Bi, Plasmon-induced hole-depletion layer on hematite nanoflake photoanodes for highly efficient solar water splitting, *Nano Energy* 35 (2017) 171–178.

[48] J. Fu, Q. Xu, J. Lov, C. Jiang, J. Yu, Ultrathin 2D/2D WO<sub>3</sub>/g-C<sub>3</sub>N<sub>4</sub> step-scheme H<sub>2</sub>-production photocatalyst, *Appl. Catal. B: Environ.* 243 (2019) 556–565.

[49] T.W. Kim, K.-S. Choi, Improving stability and photoelectrochemical performance of BiVO<sub>4</sub> photoanodes in basic media by adding a ZnFe<sub>2</sub>O<sub>4</sub> layer, *J. Phys. Chem. Lett.* 7 (2016) 447–451.

[50] F. Li, J. Li, J. Zhang, L. Gao, X. Long, Y. Hu, S. Li, J. Jin, J. Ma, NiO nanoparticles anchored on phosphorus-doped alpha-Fe<sub>2</sub>O<sub>3</sub> nanoarrays: an efficient hole extraction p-n heterojunction photoanode for water oxidation, *ChemSusChem* 11 (2018) 2156–2164.

[51] Y. Liu, Y. Guo, L.T. Schelhas, M. Li, J.W. Ager, Undoped and Ni-doped CoO<sub>x</sub> surface modification of porous BiVO<sub>4</sub> photoelectrodes for water oxidation, *J. Phys. Chem. C* 120 (2016) 23449–23457.

[52] X. Zhu, N. Guijarro, Y. Liu, P. Schouwink, R.A. Wells, F. Le Formal, S. Sun, C. Gao, K. Sivila, Spinel structural disorder influences solar-water-splitting performance of ZnFe<sub>2</sub>O<sub>4</sub> nanorod photoanodes, *Adv. Mater.* 30 (2018) 1801612.

[53] Y. Abbas, Z. Zuhra, N. Akhtar, S. Ali, J.R. Gong, Single-step fabrication of visible-light-active ZnO-GaN: ZnO branched nanowire array photoanodes for efficient water splitting, *ACS Appl. Energy Mater.* 1 (2018) 3529–3536.

[54] K. Zhang, T. Dong, G. Xie, L. Guan, B. Guo, Q. Xiang, Y. Dai, L. Tian, A. Batool, S.U. Jan, R. Boddula, A.A. Thebo, J.R. Gong, Sacrificial interlayer for promoting charge transport in hematite photoanode, *ACS Appl. Mater. Interfaces* 9 (2017) 42723–42733.

[55] B. Guo, L. Tian, W. Xie, A. Batool, G. Xie, Q. Xiang, S.U. Jan, R. Boddula, J.R. Gong, Vertically aligned porous organic semiconductor nanorod array photoanodes for efficient charge utilization, *Nano Lett.* 18 (2018) 5954–5960.

[56] J. Xiao, X. Hou, L. Zhao, Y. Li, A carbon-quantum-dot-sensitized ZnO:Ga/ZnO multijunction composite photoanode for photoelectrochemical water splitting under visible light irradiation, *J. Catal.* 346 (2017) 70–77.

[57] C. Li, A. Li, Z. Luo, J. Zhang, X. Chang, Z. Huang, T. Wang, J. Gong, Surviving high-temperature calcination: ZrO<sub>2</sub>-Induced hematite nanotubes for photoelectrochemical water oxidation, *Angew. Chem. Int. Ed.* 56 (2017) 4150–4155.

[58] W. He, Y. Yang, L. Wang, J. Yang, X. Xiang, D. Yan, F. Li, Photoelectrochemical water oxidation efficiency of a core/shell array photoanode enhanced by a dual suppression strategy, *ChemSusChem* 8 (2015) 1568–1576.

[59] B. He, Y. Wang, X. Liu, Y. Li, X. Hu, J. Huang, Y. Yu, Z. Shu, Z. Li, Y. Zhao, Spatial engineering of a Co(OH)<sub>x</sub> encapsulated p-Cu<sub>2</sub>S/n-BiVO<sub>4</sub> photoanode: simultaneously promoting charge separation and surface reaction kinetics in solar water splitting, *J. Mater. Chem. A* 7 (2019) 6747–6752.

[60] M. Zeng, X. Peng, J. Liao, G. Wang, Y. Li, J. Li, Y. Qin, J. Wilson, A. Song, S. Lin, Enhanced photoelectrochemical performance of quantum dot-sensitized TiO<sub>2</sub> nanotube arrays with Al<sub>2</sub>O<sub>3</sub> overcoating by atomic layer deposition, *Phys. Chem. Chem. Phys.* 18 (2016) 17404–17413.

[61] B. Guo, A. Batool, G. Xie, R. Boddula, L. Tian, S.U. Jan, J.R. Gong, Facile integration between Si and catalyst for high-performance photoanodes by a multifunctional bridging layer, *Nano Lett.* 18 (2018) 1516–1521.

[62] W. Li, K.R. Yang, X. Yao, Y. He, Q. Dong, G.W. Brudvig, V.S. Batista, D. Wang, Facet-dependent kinetics and energetics of hematite for solar water oxidation reactions, *ACS Appl. Mater. Interfaces* 11 (2019) 5616–5622.

[63] L. Wang, Z. Wang, X. Mao, P. Chen, M. Xiao, S.A. Monny, S. Wang, M. Konarova, A. Du, Understanding the roles of oxygen vacancy in hematite based photoelectrochemical process, *Angew. Chem. Int. Ed.* 131 (2019) 1042–1046.

[64] Y. Tang, X. Fang, X. Zhang, G. Fernandes, Y. Yan, D. Yan, X. Xiang, J. He, Space-confined earth-abundant bifunctional electrocatalyst for high-efficiency water splitting, *ACS Appl. Mater. Interfaces* 9 (2017) 36762–36771.

[65] H. Zhang, C. Cheng, Three-dimensional FTO/TiO<sub>2</sub>/BiVO<sub>4</sub> composite inverse opals photoanode with excellent photoelectrochemical performance, *ACS Energy Lett.* 2 (2017) 813–821.

[66] F. Wu, Q. Liao, F. Cao, L. Li, Y. Zhang, Non-noble bimetallic NiMoO<sub>4</sub> nanosheets integrated Si photoanodes for highly efficient and stable solar water splitting, *Nano Energy* 34 (2017) 8–14.